Extreme Mechanics Letters 45 (2021) 101277

Contents lists available at ScienceDirect

Extreme Mechanics Letters

journal homepage: www.elsevier.com/locate/eml

A poro-damage phase field model for hydrofracturing of glacier crevasses

Xiangming Sun [a], Ravindra Duddu [a,*], Hirshikesh [b]

[a] Department of Civil and Environmental Engineering, Vanderbilt University, Nashville, TN, 37235, USA
[b] Department of Mechanical Engineering, Indian Institute of Technology Madras, Chennai, 600036, India

ARTICLE INFO

Article history:
Received 4 January 2021
Received in revised form 16 February 2021
Accepted 7 March 2021
Available online 13 March 2021

Keywords:
Hydrofracture
Phase field model
Poro-damage mechanics
Glacier crevasses
Iceberg calving

ABSTRACT

Hydraulic fracture (or hydrofracture) can promote the propagation of meltwater-filled surface crevasses in glaciers and, in some cases, lead to full-depth penetration that can enhance basal sliding and iceberg calving. Here, we propose a novel poro-damage phase field model for hydrofracturing of glacier crevasses, wherein the crevasse is represented by a nonlocal damage zone and the effect of hydrostatic pressure due to surface meltwater is incorporated based on Biot's poroelasticity theory. We find that the elastic strain energy decomposition scheme of Lo et al. (2019) with an appropriate fracture energy threshold can adequately represent the asymmetric tensile–compressive fracture behavior of glacier ice subjected to self-gravity loading. We assessed the performance of the model against analytical linear elastic fracture mechanics solutions by comparing their predictions of maximum crevasse penetration depth. The model simulates both surface crevasse propagation in the interior region of the glacier, as well as cliff failure in the terminus region. The excellent performance of the proposed model for air/water-filled surface crevasses in idealized land- and marine-terminating grounded glaciers illustrates its applicability to studying the dynamic response of glaciers to atmospheric warming.

1. Introduction

Surface crevasses are predominantly mode I fractures and are ubiquitous in both Antarctic and Greenland glaciers [1]. Some crevasses are extreme-scale fractures penetrating tens of meters deep into glaciers that are hundreds of meters thick; whereas most crevasses are relatively shallow (<10 m deep) [2], as the longitudinal stress in glacier ice subjected to self-gravity loading changes from tensile to compressive at lower depths. Meltwater in surface crevasses can apply hydraulic pressure on crevasse walls and promote crevasse growth deeper into the glacier, a process that is often referred to as hydrofracture. Under certain conditions, water-filled crevasses can penetrate through the full thickness of the glacier leading to iceberg calving [3–5] and enhance basal sliding by altering subglacial hydrology [6–8]. In fact, hydrofracture occurs at tens of thousands of sites on the Greenland ice sheet each summer, and its occurrence is increasing with atmospheric warming [9]. However, the physical factors (e.g. glacier geometry, stress state, basal and terminus boundary conditions) enabling the full-depth propagation of hydrofractures at these sites are poorly understood. It is crucial that we investigate these physical factors to better understand iceberg calving, which is one of the most enigmatic glaciological processes. Advanced models for representing or parametrizing hydrofracture-driven iceberg calving in ice sheet models [10] are essential to reduce the large uncertainty in future sea level rise projections [11]. With this in mind, we develop a phase field model for hydrofracture of meltwater-filled surface crevasses by extending the notion of poro-damage mechanics [12,13].

Over shorter time scales of crevasse propagation, glacier ice can be assumed to behave like a compressible linear elastic solid, which is supported by observations of fracture propagation in Icelandic glaciers [14]. Therefore, in the field of glaciology, analytical linear elastic fracture mechanics (LEFM) models [3,4,15,16] are commonly used to estimate the penetration depth of crevasses and predict iceberg calving [17–19]. However, analytical LEFM models rely on weight functions to evaluate the stress intensity factor that are applicable for idealized geometries (e.g. rectangular plates) and boundary conditions (e.g. traction free or symmetric edge), so their relevance to iceberg calving of real glaciers and ice shelves is somewhat limited [20]. Moreover, analytical LEFM models only describe crack propagation, so *ad hoc* criteria are often necessary to describe when/where a crack will nucleate, and how much and in which direction it will propagate [21], but these criteria can alter crack trajectories and may lead to non-physical outcomes [22,23]. Despite advances in the numerical implementations of LEFM models [24–

* Corresponding author.
E-mail address: ravindra.duddu@vanderbilt.edu (R. Duddu).

https://doi.org/10.1016/j.eml.2021.101277
2352-4316/

28], the underlying algorithms can be cumbersome and simulating crack branching and coalescence is challenging, which limits their usability in practice.

To address the shortcomings of the LEFM models, the phase field model (PFM) for fracture was introduced in the seminal works of [21,29] that describes crack propagation in solids by minimizing the total potential energy based on Griffith's theory [30]. The PFM for fracture can be categorized as a nonlocal continuum damage model, and as such it enables robust simulation of complex crack growth, including crack initiation, propagation, as well as branching and merging. For brittle fracture, the crack is defined by a diffused damage zone and material failure is characterized by a constitutive damage relation arising from variational [29] or thermodynamical arguments [31]. A major limitation of the PFM is the difficulty in capturing asymmetric damage growth under multi-axial, mixed-mode, and tensile–compressive stress states. To avoid the growth of damage under compression in PFMs and inter-penetration of crack surfaces, *ad hoc* approaches were proposed based on: volumetric/deviatoric split of strain energy [32], spectral decomposition (positive/negative split) of strain tensor [33]. Efficient hybrid formulations were also proposed with spectral decomposition of strain tensor applied only to damage evolution under tension [34].

In the past few years, numerous extensions and advanced implementations of PFMs for dynamic, cohesive and fatigue crack propagation have been developed [35–38]. A comprehensive review of these developments is beyond the scope of this paper, so here we limit the discussion to a few articles that proposed improvements to crack driving force functions for describing fracture under mixed-mode, compression–shear, and/or hydraulic loadings. Zhang et al. [39] proposed normalizing the volumetric and deviatoric part of the strain energy with fracture energies under pure mode I (opening) and mode II (sliding) loading, respectively, to define the crack driving force under mixed-mode loading, which was later extended to anisotropic rocks in [40]. However, this energy splitting approach can still unphysically evolve damage under certain stress states with all negative principal stresses [41] and may not capture the crack boundary conditions correctly under compression and shear [42]. Wang et al. [43] implemented a strain energy decomposition scheme based on maximum normal and shear stresses criteria to handle mixed-mode fracture, wherein the direction of crack propagation can be determined based on the unified tensile fracture criterion. Zhou et al. [44] proposed a crack driving force function to capture compression–shear fractures in rock-like materials that was validated with uniaxial compression tests.

Seemingly, the first-ever PFM for simulating hydraulic fracturing in linear elastic impermeable materials was developed by Bourdin et al. [45]. Mikelić et al. [46] further extended this PFM for simulating fluid-driven fracture propagation in saturated poroelastic medium, wherein the fluid flow inside cracks is assumed to obey the lubrication theory, while that in the bulk region obeys Darcy's law and Biot equations of poroelasticity. Subsequently, several PFMs were proposed to simulate hydraulic fracture in poroelastic media [13,47–53]. However, the aforementioned PFMs were proposed to model the process of hydrofracturing or fracking in unconventional oil and natural gas industry, which involves the injection of fluid at high pressure. In contrast, hydrofracture of water-filled crevasses in glaciers can occur without the pressurized injection of water. For example, the slow accumulation of melted surface water in the crevasses can trigger hydrofracture owing to the density difference between ice (917 kg/m^3) and fresh water (1000 kg/m^3) and the low fracture toughness of ice (0.1 MPa $\sqrt{\text{m}}$). Thus, water-filled crevasses can initiate at low pressures and propagate in a quasi-static, episodic manner in glaciers, and sometimes may cease to propagate and freeze up during winter months [9]. Therefore, it is reasonable to assume that meltwater pressure in crevasses is hydrostatic and utilize our poro-damage approach [12,54], and bypass modeling fluid flow in the crevasse.

The purpose of this paper is to establish a thermodynamically-consistent alternative to the nonlocal continuum poro-damage mechanics model for hydrofracturing of glacier crevasses [54]. This will enable us to systematically study and understand the physical factors at certain sites leading to full depth propagation of crevasses and drainage of supraglacial lakes. The rest of the paper is organized as follows: in Section 2, we review the phase field formulation for brittle fracture, extend it to simulate quasi-static hydrofracture based on the notion of poro-damage mechanics, and implement the extended PFM based on staggered numerical solution strategy; in Section 3, we compare the predictions of crevasses depths for grounded glaciers using the PFM against that using the LEFM models, and demonstrate the capability of the PFM for simulating self-sustaining retreat of the ice terminus; in Section 4, we conclude with a brief summary and closing remarks.

2. Model formulation

In this section, we first review the fundamental concepts of the phase field model (PFM), where brittle fracture is described by a scalar order parameter, that is, the phase-field/damage variable. We next propose modified phase field model for hydrofracture based on the notion of poro-damage mechanics that incorporates hydrostatic pressure within the cracks and voids situated in the nonlocal damage zone. We then summarize the strong form of the governing equations of the poro-damage PFM for quasi-static hydrofracture along with the respective boundary conditions. Finally, we describe the operator-splitting strategy adopted by the hybrid formulation of the PFM.

2.1. Review of phase field model for brittle fracture

The phase field model generally approximates the isotropic damage state of a material point at position $\mathbf{x}$ and time t using the scalar (phase-field) variable $D(\mathbf{x}, t) \in [0, 1]$, such that $D = 0$ represents undamaged state and $D = 1$ the fully damaged state. According to Griffith's theory of brittle fracture [30], the total energy stored in a cracked solid body $\Omega \subset \mathbb{R}^2$ includes internal (Ψ_{int}) and external (Ψ_{ext}) components. The regularized form of this total energy Ψ can be expressed as

$$\Psi = \overbrace{\underbrace{\int_\Omega \psi_{\text{e}}(\boldsymbol{\varepsilon}, D)\, \mathrm{d}\Omega}_{\Psi_{\text{E}}} + \underbrace{\int_\Omega \mathcal{G}_{\text{c}}\gamma\,(D, \nabla D)\; \mathrm{d}\Omega}_{\Psi_{\text{D}}}}^{\Psi_{\text{int}}} - \overbrace{\int_\Omega \boldsymbol{b}\cdot\boldsymbol{u}\, \mathrm{d}\Omega - \int_{\partial\Omega_{\text{t}}} \boldsymbol{t}^*\cdot\boldsymbol{u}\, \mathrm{d}\Gamma}^{\Psi_{\text{ext}}}, \tag{1}$$

where Ψ_{E} is the elastic energy of the solid, Ψ_{D} is the fracture energy needed for the propagation of the crack interface, ψ_{e} is the elastic strain energy density function, $\boldsymbol{\varepsilon}$ is the small strain tensor, $\mathcal{G}_{\text{c}}$ is the critical strain energy release rate, γ is the crack surface density function, ∇ is the spatial gradient operator, $\boldsymbol{b}$ is the body force, $\boldsymbol{u}$ is the displacement vector, and $\boldsymbol{t}^*$ is the traction applied to the external boundary $\partial\Omega_{\text{t}}$.

For isotropic linear elasticity, the strain energy density function of the undamaged (or intact) material ψ_{e}^0 is defined as

$$\psi_{\text{e}}^0(\boldsymbol{\varepsilon}) = \frac{\lambda}{2}\,[\text{tr}(\boldsymbol{\varepsilon})]^2 + \mu\,\text{tr}(\boldsymbol{\varepsilon}^2), \tag{2}$$

where λ and μ are the Lamé parameters that can be calculated using Young's modulus E and Poisson's ratio ν. In the phase field formulation for fracture, the strain energy density function of damaged material ψ_e can be approximated as

$$\psi_e(\boldsymbol{\varepsilon}, D) = g_d(D)\psi_e^0(\boldsymbol{\varepsilon}), \tag{3}$$

where we assume the quadratic degradation function $g_d = (1 - D)^2$. The Cauchy stress tensor can be derived as

$$\boldsymbol{\sigma} = \frac{\partial \psi_e}{\partial \boldsymbol{\varepsilon}} = g_d(D)\left[\lambda \mathrm{tr}(\boldsymbol{\varepsilon})\boldsymbol{I} + 2\mu\boldsymbol{\varepsilon}\right], \tag{4}$$

where $\boldsymbol{I}$ represents the identity tensor. However, Eq. (3) may lead to physically unrealistic energy release owing to the symmetric treatment of fracture in both tension and compression. To remedy this issue, Miehe et al. [31] proposed an *ad hoc* additive decomposition of the elastic strain energy density and modified Eq. (3) as

$$\psi_e(\boldsymbol{\varepsilon}, D) = g_d(D)\psi_e^+(\boldsymbol{\varepsilon}) + \psi_e^-(\boldsymbol{\varepsilon}), \tag{5}$$

where ψ_e^+ and ψ_e^- represent the contributions to the elastic strain energy from tensile and compressive strain states. The Cauchy stress tensor based on this strain energy decomposition is

$$\boldsymbol{\sigma} = \frac{\partial \psi_e}{\partial \boldsymbol{\varepsilon}} = g_d(D)\frac{\partial \psi_e^+}{\partial \boldsymbol{\varepsilon}} + \frac{\partial \psi_e^-}{\partial \boldsymbol{\varepsilon}}. \tag{6}$$

In the framework of the phase field theory for brittle fracture proposed by Miehe et al. [33], the crack surface density per unit volume of the solid is given by

$$\gamma(D, \nabla D) = \frac{D^2}{2\ell_c} + \frac{\ell_c}{2}|\nabla D|^2, \tag{7}$$

where ℓ_c is the length scale parameter that controls the width of the diffuse crack interface. Although the appropriate choice of ℓ_c can provide experimentally supported crack growth prediction [55], it is often treated as a numerical (damage) parameter. The time evolution of phase-field variable can be obtained by minimizing the total potential energy functional as

$$\eta\dot{D} = \frac{\partial \Psi}{\partial D} - \nabla \cdot \left(\frac{\partial \Psi}{\partial \nabla D}\right) = \ell_c \Delta D - \frac{D}{\ell_c} + 2(1 - D)\frac{\mathcal{H}}{\mathcal{G}_c}, \tag{8}$$

where $\Delta = \nabla \cdot \nabla$ is the Laplace operator, η is the viscous regularization parameter defined for numerical stabilization, and $\mathcal{H}$ is the history field variable that ensures monotonic increase of the phase-field variable (i.e. irreversible damage neglecting any healing). Here we evaluate three different schemes proposed in the literature for calculating the history field variable:

***Miehe's scheme*:** To describe brittle tensile fracture, Miehe et al. defined the history field variable as [33]

$$\mathcal{H}(\mathbf{x}, t) = \max_{\tau \in [0,t]} \psi_e^+(\boldsymbol{\varepsilon}(\mathbf{x}, \tau)), \tag{9}$$

where the positive component of elastic strain energy ψ_e^+ is given by

$$\psi_e^+(\boldsymbol{\varepsilon}) = \frac{\lambda}{2}\langle \mathrm{tr}(\boldsymbol{\varepsilon})\rangle^2 + \mu \mathrm{tr}(\langle \boldsymbol{\varepsilon}\rangle^2), \tag{10}$$

and $\langle \cdot \rangle = (\cdot + |\cdot|)/2$ denotes the Macaulay's bracket. As noted by Lo et al. [38], Miehe's scheme does not guarantee the prohibition of damage accumulation in compressive regions due to Poisson's ratio effects in three-dimensions.

***Zhang's scheme*:** To handle mixed-mode fracture, Zhang et al. defined the history field variable based on Miehe's scheme as [39]

$$\mathcal{H}(\mathbf{x}, t) = \max_{\tau \in [0,t]} \left(\frac{\mathcal{H}_\mathrm{I}(\mathbf{x}, \tau)}{\mathcal{G}_\mathrm{Ic}} + \frac{\mathcal{H}_\mathrm{II}(\mathbf{x}, \tau)}{\mathcal{G}_\mathrm{IIc}}\right)\mathcal{G}_c, \tag{11}$$

where $\mathcal{H}_\mathrm{I} = \frac{\lambda}{2}\langle \mathrm{tr}(\boldsymbol{\varepsilon})\rangle^2$ and $\mathcal{H}_\mathrm{II} = \mu \mathrm{tr}(\langle \boldsymbol{\varepsilon}\rangle^2)$ are history field variables contributing to mode I and mode II fracture, respectively. Notably, Zhang's scheme based on Eq. (11) recovers Miehe's scheme when $\mathcal{G}_\mathrm{IIc}$ is taken as the same as $\mathcal{G}_\mathrm{Ic}$, which is rarely the case for most brittle materials.

***Lo's scheme*:** To ensure that compressive stress states do not contribute to crack/damage growth, Lo et al. [38] proposed a different decomposition scheme in three dimensions. Here, we adapt this formulation for the two-dimensional (2-D) plane strain case as:

$$\begin{cases} \textbf{if } \varepsilon_1 \geq \varepsilon_2 \geq 0, \\ \quad \textbf{then } \psi_e^+ = \frac{\lambda}{2}(\varepsilon_1 + \varepsilon_2)^2 + \mu(\varepsilon_1^2 + \varepsilon_1^2); \\ \textbf{elseif } \varepsilon_1 \geq 0 \geq \varepsilon_2 \textbf{ and } (1 - \nu)\varepsilon_1 + \nu\varepsilon_2 > 0, \\ \quad \textbf{then } \psi_e^+ = \dfrac{E\left[(1 - \nu)\varepsilon_1 + \nu\varepsilon_2\right]^2}{2(1 - 2\nu)(1 - \nu^2)}; \\ \textbf{else } \psi_e^+ = 0. \end{cases} \tag{12}$$

where $\varepsilon_1 \geq \varepsilon_2$ are taken as the ordered principal strains. The history field variable can then be updated using Eq. (9).

2.2. Poro-damage phase field model for quasi-static hydrofracture

We extend the PFM formulation using the notion of poro-damage mechanics to simulate the propagation of meltwater-filled crevasses in glaciers; however, it is also applicable to simulate fluid-filled fractures in geological media subjected to self-gravitation loads. As depicted in Fig. 1, the specific physical problem consists of a glacier crevasse filled with either air or meltwater depending on the water level within the damaged region ($D > 0$). Because the crevasse opening is much small compared to the glacier length, we can approximate it as a thin, finite-thickness damage zone. Because the glacier thickness is smaller compared to its length and width, we consider the plane strain approximation to simulate the crevasse problem in 2-D, which also reduces the computational burden. Five different physical representative volume elements (RVE) can be conceived to exist in the glacier domain to describe all the possible scenarios. Fig. 1(a) shows an intact physical RVE ($D = 0$) that is far away from the crevassed or damaged region. Fig. 1(b) and (d) show the partially damaged physical RVEs ($0 < D < 1$) where smaller voids and cracks are filled with air and water, respectively. Fig. 1(c) and (e) show the fully damaged physical RVEs ($D = 1$) representing air-filled and water-filled crack openings that are located above and beneath the water level, respectively.

To account for the effect of hydrostatic pressure of meltwater on surface crevasse propagation, we interpret the damaged region of the crevasse beneath the water level as a fluid-saturated poroelastic medium. According to this poro-damage interpretation, the total internal energy stored in this region can then be defined as

$$\Psi_\mathrm{int} = \Psi_\mathrm{E} + \Psi_\mathrm{D} + \Psi_\mathrm{F}, \tag{13}$$

where Ψ_F is the potential energy stored in the fluid. In the fully damaged region Ω_D of the diffuse damage zone, the potential energy stored in the fluid (water) can be defined as [46]

$$\Psi_\mathrm{F} = \int_{\Omega_\mathrm{D}} \psi_\mathrm{f}(p, \nabla \cdot \boldsymbol{u})\ \mathrm{d}\Omega, \tag{14}$$

where p is the fluid/poroelastic pressure, and ψ_f the potential energy density of the fluid. We assume meltwater within the crevasse to be flowing slow enough and at times stagnant, so that the hydrostatic condition applies. In other words, we assume the fluid/poroelastic pressure p within the fully damaged region is equal to the hydrostatic pressure p_w. Because we are primarily interested in predicting the maximum crevasse depth of water-filled crevasses, it is reasonable to simplify the model by assuming hydrostatic conditions, thereby neglecting the fluid

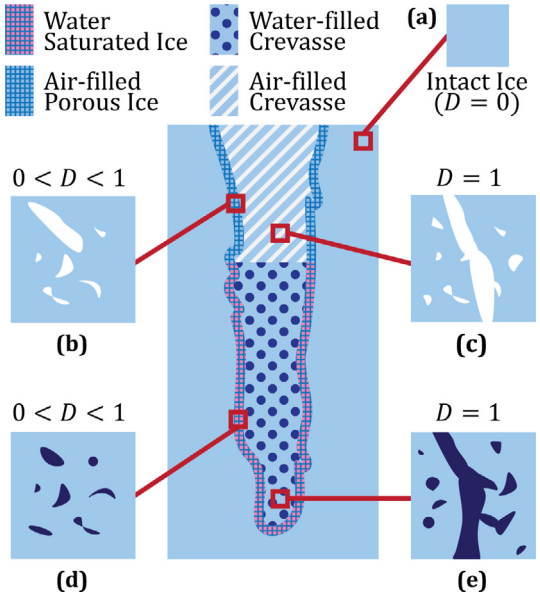

Fig. 1. Schematic illustration of the damaged glacier. The fully damaged region ($D = 1$) of the crevasse is filled with either air or water depending on the assumed water level within the crevasse. The principal planes of the physical representative volume elements (RVE) for (a) intact ice ($D = 0$); (b) cracking ice with air-filled microcracks and microvoids ($0 < D < 1$); (c) air-filled broken ice ($D = 1$); (d) water saturated cracking ice ($0 < D < 1$); (e) water-filled broken ice ($D = 1$).

flow within the damage zone. The potential energy density of the fluid inside Ω_D can then be calculated as

$$\psi_f(p, \nabla \cdot \boldsymbol{u}) = -p\alpha \nabla \cdot \boldsymbol{u} = -p_w \alpha \mathrm{tr}(\boldsymbol{\varepsilon}), \tag{15}$$

where α is the Biot coefficient. The hydrostatic pressure within the damaged region can be simply determined based on the water depth at a specific position z as

$$p_w(z) = \rho_f g \langle h_s - (z - z_s) \rangle, \tag{16}$$

where ρ_f is the density of freshwater, g the gravitational acceleration, h_s the water level of crevasses, and z_s the location of the crevasse tip.

Note that the integral in Eq. (14) is defined over the fully damaged region Ω_D, which changes in size as the crevasse propagates. To account for the effect of fluid/poroelastic pressure in the entire diffuse-crack region ($0 < D \leq 1$), we modify Eq. (15) as

$$\psi_f(p, \nabla \cdot \boldsymbol{u}, D) = -g_f(D) p_w \alpha \nabla \cdot \boldsymbol{u}, \tag{17}$$

where $g_f(D) = 1 - g_d(D)$ is an interpolation function that satisfies three conditions as

$$g_f(0) = 0, \; g_f(1) = 1, \; g_f'(1) = 0. \tag{18}$$

The first condition indicates that no fluid energy is stored in the intact elastic medium, which contains no cracks or voids. The second condition ensures that Eq. (17) reduces to Eq. (14) in the fully-damaged region (i.e. $D = 1$). The third condition ensures that the crack driving force vanishes as the phase-field variable converges to one. Thus, Eq. (17) allows us to define the integral in Eq. (14) over the whole domain Ω, instead of just over Ω_D.

We employ the hybrid approach to solve the phase field formulation for hydrofracture, wherein the elastic strain energy decomposition is used only for the calculation of the history field variable $\mathcal{H}$. Therefore, the Cauchy stress tensor in the poro-damage PFM is defined as

$$\boldsymbol{\sigma} = \frac{\partial \psi}{\partial \boldsymbol{\varepsilon}} = \frac{\partial \psi_e}{\partial \boldsymbol{\varepsilon}} + \frac{\partial \psi_f}{\partial \boldsymbol{\varepsilon}} = g_d(D)\left[\lambda \mathrm{tr}(\boldsymbol{\varepsilon})\boldsymbol{I} + 2\mu\boldsymbol{\varepsilon}\right] - g_f(D) p_w \alpha \boldsymbol{I}. \tag{19}$$

To further regularize the formulation, we modify the above constitutive relation as

$$\boldsymbol{\sigma} = \max\left(g_d(D), \kappa\right)\left[\lambda \mathrm{tr}(\boldsymbol{\varepsilon})\boldsymbol{I} + 2\mu\boldsymbol{\varepsilon}\right] - g_f(D) p_w \alpha \boldsymbol{I}, \tag{20}$$

where $\kappa = 10^{-6}$ is small regularization parameter. Note that the expression $\max\left(g_d(D), \kappa\right)$ can be alternatively expressed as $(1 - \kappa) g_d(D) + \kappa$ [44]. The phase field evolution equation can be obtained by minimizing the modified total potential energy functional as

$$\eta \dot{D} = \ell_c \Delta D - \frac{D}{\ell_c} + 2(1 - D)\frac{\mathcal{H}}{\mathcal{G}_c}, \tag{21}$$

where the history variable including the effect of fluid/poroelastic pressure is given by

$$\mathcal{H}(\mathbf{x}, t) = \max_{\tau \in [0,t]} \left[\psi_e^+\left(\boldsymbol{\varepsilon}(\mathbf{x}, \tau)\right) + p_w \alpha \mathrm{tr}\left(\boldsymbol{\varepsilon}(\mathbf{x}, \tau)\right)\right]. \tag{22}$$

In summary, the above poro-damage PFM can be used to simulate the propagation of both air-filled and water-filled crevasses. For air-filled crevasses, the poroelastic pressure $p_w = 0$ everywhere within Ω, which is the case during winter months in Greenland when there is no surface meltwater. Clearly, in this case the poro-damage PFM for hydrofracture reduces to that for brittle fracture reviewed in Section 2.1.

2.3. Strong form of governing equations

The crevasse propagation problems involves solving for two unknown fields, namely the displacement field $\boldsymbol{u}$ and the phase-field (isotropic damage) variable D. The displacement field $\boldsymbol{u}$ is obtained by solving the elastostatic boundary value problem. The corresponding strong form of the static equilibrium equations and the boundary conditions are:

$$\begin{cases} \nabla \cdot \boldsymbol{\sigma} + \boldsymbol{b} = \boldsymbol{0} & \text{in } \Omega, \\ \boldsymbol{u} = \boldsymbol{u}^* & \text{on } \partial\Omega_u, \\ \boldsymbol{\sigma} \cdot \mathbf{n} = \boldsymbol{t}^* & \text{on } \partial\Omega_t, \end{cases} \tag{23}$$

where $\boldsymbol{u}^*$ represents a prescribed displacement enforced on external boundary $\partial\Omega_u$, $\mathbf{n}$ denotes the unit normal to the boundary $\partial\Omega$ pointing outward from Ω, and the Cauchy stress $\boldsymbol{\sigma}$ is defined by the constitutive Eq. (20). The body force is due to the self-gravitation load with a magnitude of $-\rho g$ in the z-direction. In the two-phase medium consisting of glacier ice and meltwater, we approximate the material density ρ based on the poro-damage interpretation as

$$\rho = (1 - D)\rho_i + D\rho_f, \tag{24}$$

where ρ_i is the density of ice. The strong form of the scalar phase field evolution equation in the rate form and the associated boundary condition are:

$$\begin{cases} \eta \dot{D} = \ell_c \Delta D - \frac{D}{\ell_c} + 2(1 - D)\frac{\mathcal{H}}{\mathcal{G}_c} & \text{in } \Omega, \\ \nabla D \cdot \mathbf{n} = 0 & \text{on } \partial\Omega. \end{cases} \tag{25}$$

The introduction of the artificial viscosity parameter η leads to a "pseudo"-time dependence of damage evolution. Therefore, the phase field equation requires an incremental time-stepping procedure to track fracture propagation, unlike the linear elastic fracture mechanics model that only defines the final crack length.

Table 1
Material properties of compressible, linear elastic ice and phase field parameters chosen in this study. The Young's modulus and Poisson's ratio of ice are assumed from [57], and the densities of glacier ice and seawater are assumed from [20].

Parameter	Symbol	Value [Unit]
Biot coefficient	α	1.0 [–]
Viscous regularization parameter	η	50 [N s/m^2]
Poisson's ratio	ν	0.35 [–]
Freshwater density	ρ_f	1000 [kg/m^3]
Ice density	ρ_i	917 [kg/m^3]
Seawater density	ρ_s	1020 [kg/m^3]
Young's modulus	E	9500 [MPa]
Gravitational acceleration	g	9.81 [m/s^2]
Length scale parameter	ℓ_c	0.625 [m]

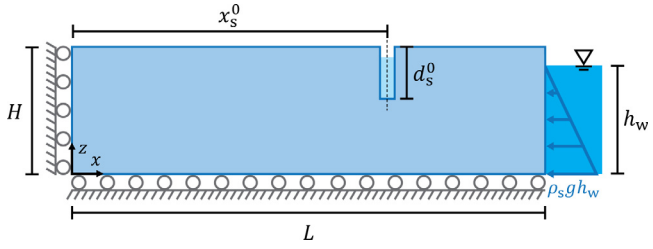

Fig. 2. Schematic diagram of marine-terminating grounded glacier with free slip at the left edge and the base. A hydrostatic load with hydraulic head h_w is applied to the right edge of the domain as a depth-varying (triangularly) distributed load. A rectangular pre-damaged zone ($D = 0.99$) with width $4\ell_c$ and depth d_s^0 is defined to initiate the propagation of surface crevasse. The horizontal distance between the left edge of the domain and the center of the pre-damaged zone is denoted by x_s^0.

2.4. Staggered solution strategy

The hybrid PFM formulation ensures damage accumulation is driven only by the tensile elastic strain energy, albeit it uses the simpler constitutive damage law for defining the Cauchy stress, which significantly reduces the computational burden [34]. This feature of the hybrid formulation allows the usage of a staggered scheme, which provides flexibility and stability compared to the monolithic scheme [44]. In this study, we employ a three-step staggered numerical solution strategy at any given pseudo time increment:

1. Compute the displacement $\boldsymbol{u}$ using static equilibrium along with its boundary conditions defined in Eq. (23) and the constitutive damage law defined by Eq. (20);
2. Evaluate the tensile elastic strain energy ψ_e^+ and/or the history variable $\mathcal{H}$ using Eq. (22), and then update the crack driving force $\mathcal{H}/\mathcal{G}_c$;
3. Compute the isotropic damage variable D by solving the phase field evolution equation (25).

We discretize and solve the governing equations of the PFM using the standard finite element method in the open-source software FEniCS [56]. The domain is spatially discretized using three-noded linear triangular finite elements. To check the accuracy of our hybrid PFM implementation, we considered the benchmark test involving a single edge cracked specimen under uniaxial tension using three different strain energy decomposition schemes introduced in Section 2.1. For more details see Appendix B.

3. Results and discussion

In this section, we use the poro-damage PFM to simulate hydrofracture of water-filled crevasses in grounded glaciers. We compare the predicted maximum crevasse depths against those obtained from the linear elastic fracture mechanics (LEFM) model detailed in Appendix C. We assume that glacier ice on smaller time scales of crevasse propagation exhibits compressible elastic behavior [14]. Material properties and related phase field parameters assumed in this study are listed in Table 1; these properties correspond to laboratory-made ice, which we used in our prior studies [54,57]. Owing to the porosity and heterogeneity of glacier ice, the material properties we assumed only represent those of ice cores extracted from lower depths [58,59].

As listed in Table 1, we take the length scale parameter $\ell_c = 0.625$ m in all the following simulation studies, unless specified otherwise. Although it is possible to conduct experiments to calibrate the phase field model (e.g. [55]), it is quite challenging to conduct experiments on glacier or polycrystalline ice due to its low melting point and low tensile strength, which requires specialized equipment and laboratory infrastructure. Owing to the lack of detailed experiments, we resort to simple estimates for the length scale parameter. According to Hillerborg et al. [60], ℓ_c is indicative of the size of the fracture/damage process zone ahead of the crack tip and can be related to the cohesive strength σ_c as

$$\ell_c \approx \frac{E\mathcal{G}_{Ic}}{\sigma_c^2} = \frac{(1-\nu^2)K_{Ic}^2}{\sigma_c^2}, \tag{26}$$

where K_{Ic} is the critical stress intensity factor (SIF) for mode I fracture. For the glacier ice, the stress intensity factor can be obtained from chevron notch tests conducted by Rist et al. [61], and cohesive strength can be assumed based on the range suggested by previous studies on glacier ice [4,17]. Thus, taking $K_{Ic} = 0.1$ MPa $\sqrt{\text{m}}$ and cohesive strength $\sigma_c = 0.1185$ MPa, we get $\ell_c \approx 0.625$ m. We also tested our model with a smaller length scale parameter (i.e., larger cohesive strength) and find that the choice of the length scale parameter does not affect the predicted maximum crevasse depth, although it alters the width of the damage zone and nucleation of damage elsewhere. From a glacier mechanics perspective, crevasse depth is the most important variable as it reveals the limits of iceberg calving, so the assumed value of ℓ_c is reasonable.

3.1. Idealized land/marine-terminating grounded glaciers

We consider a rectangular glacier domain of length $L = 500$ m and height $H = 125$ m under the plane strain assumption. As shown in Fig. 2, the free slip boundary condition is enforced at the left and bottom edges of the domain (indicated by rollers). We use the Cartesian coordinate system with $(x_1, x_2, x_3) = (x, y, z)$, where x and z represent in-plane horizontal and vertical coordinates, respectively; and the direction of y-axis must point into the x-z plane to obey the right-handed rule. The origin is set at the lower-left corner of the glacier. We consider a varying seawater depth h_w at the terminus (i.e. the right edge) of the grounded glacier. In the case of land-terminating glacier (i.e. $h_w = 0$), the zero traction boundary condition is naturally enforced at the glacier terminus. In the case of a marine-terminating grounded glacier (i.e., $h_w > 0$), hydrostatic pressure with hydraulic head h_w is applied at the glacier terminus as a depth-varying (triangularly) distributed load. To simulate the propagation of a single isolated surface crevasse in the glacier and compare the result with the LEFM model, we prescribe a rectangular pre-damaged zone ($D = 0.99$) with $4\ell_c$ in width and d_s^0 in depth. The horizontal distance between the left edge of the domain and the center of the pre-damaged zone is denoted by x_s^0.

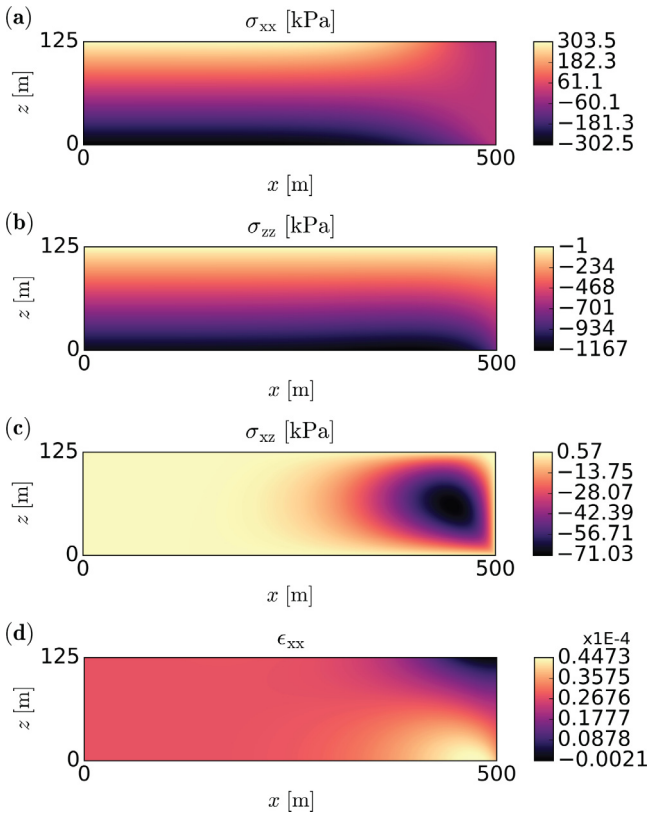

Fig. 3. Stress and strain states of pristine land-terminating glaciers under plane strain assumptions using the finite element method (FEM): (a) σ_{xx}: normal stress in x-direction; (b) σ_{zz}: normal stress in z-direction; (c) σ_{xz}: shear stress in x-z plane; (d) ε_{xx}: normal strain in x-direction.

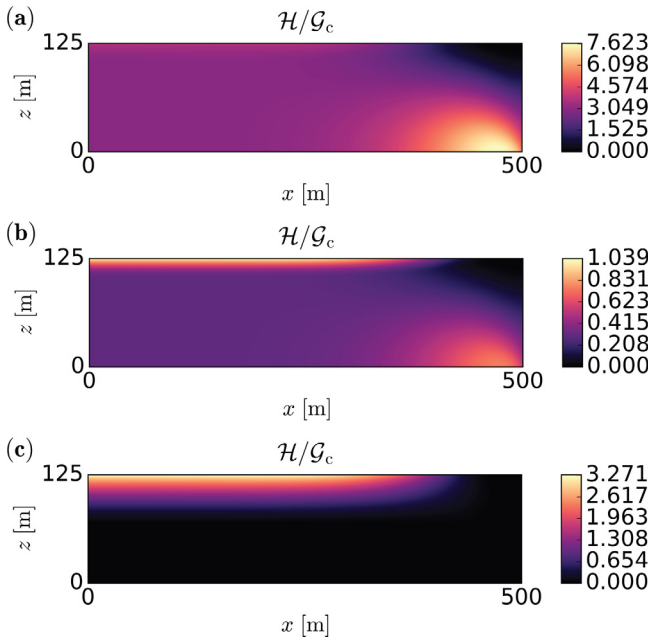

Fig. 4. Crack driving force of pristine land-terminating glaciers $\mathcal{H}/\mathcal{G}_c$ using three different strain energy decomposition schemes proposed by: (a) Miehe et al. [33]; (b) Zhang et al. [39]; (c) Lo et al. [38].

3.2. Stress state and crack driving force

We first evaluate the stress state in a land-terminating glacier (i.e., $h_w = 0$) without any pre-damaged zone. As per the plane strain assumption, we have three independent components of the Cauchy stress tensor, including two normal stress components and one shear stress component in the x-z plane, which are plotted in Fig. 3(a)–(c). The traction-free condition at the terminus leads to non-uniformity in normal stress components, but this free boundary/edge effect diminishes in the far-field region (i.e. away from the terminus). Consequently, the normal stress components in the far-field region do not vary in the longitudinal (x) direction and vary linearly in the vertical (z) direction. In contrast, the in-plane shear stress in the far-field region is negligibly small; whereas near the terminus it shows some non-uniform distribution. Furthermore, the far-field longitudinal stress σ_{xx} is tensile (i.e. positive) near the top surface and linearly changes to compressive (i.e. negative) with depth. The far-field stresses in Fig. 3 are consistent with the elasticity stress solutions derived in Appendix A, which partly verifies our finite element implementation in FEniCS. Because most crevasses are mode I (opening) vertical fractures driven by tensile stress, they cannot propagate beyond a certain depth where the longitudinal stress becomes zero. Also, due to the self-gravitational load of glaciers, the vertical stress σ_{yy} is compressive (i.e. negative) everywhere.

We next calculate the crack driving force in the undamaged land-terminating glacier using the three strain energy decomposition schemes described in Section 2.1. As shown in Fig. 4(a), the maximum crack driving force computed from Miehe's scheme is at the bottom surface of the near-terminus region. The maximum crack driving force computed from Zhang's scheme is at the top surface of the far-field region, as shown in Fig. 4(b). However, with Zhang's scheme we notice that the crack driving force at the bottom surface of the near-terminus region is still relatively larger than that at the surrounding area. Furthermore, the disparity in the magnitudes of crack driving forces computed from Miehe and Zhang schemes is quite significant. Regardless of the differences, the major concern is that both Miehe's and Zhang's schemes lead to finite crack driving force in regions where longitudinal normal stress σ_{xx} is negative, so they predict fracture nucleation and propagation in the most compressive regions of the glacier. This contradicts the results of the linear elastic fracture mechanics model for mode I fracture and violates the condition that damage should only evolve on in the tensile regions.

To further clarify the issue with Miehe's and Zhang's schemes, we calculate the in-plane horizontal strain of the land-terminating glacier. As shown in Fig. 3(d), the longitudinal strain ε_{xx} is positive almost everywhere; whereas the longitudinal stress σ_{xx} becomes negative with depth in the far-field region, as shown in Fig. 3(b). Because the vertical strain ε_{zz} must be negative everywhere due to the self-gravitational load, the longitudinal strain must be positive everywhere due to the Poisson's ratio effect. According to Eqs. (9) and (11), the history field variable is dictated by the trace of $\langle \boldsymbol{\varepsilon} \rangle^2$, which is positive everywhere as the longitudinal strain is positive everywhere. This explains why the crack driving force evaluated using Miehe's and Zhang's schemes are positive in the regions where the longitudinal stress σ_{xx} is compressive. This is a fundamental limitation of these two schemes that restricts its applicability to geological media subjected to self-gravitational load. To ensure that the compressive longitudinal stress does not contribute to mode I fracture nucleation or propagation, Lo et al. introduced a modified scheme applicable for masonry-like materials that exhibit tension–compression asymmetry [38]. As shown in Fig. 4(c), the crack driving force obtained from the Lo's scheme is zero in the regions where the longitudinal stress is negative, and is maximum at the top surface in the far-field region where the longitudinal stress is positive. Thus, we find that only the Lo's scheme provides a consistent description of

mode I fracture compared to the LEFM model by accounting for the tension–compression asymmetry of glacier ice subjected to self-gravitational load.

3.3. Damage evolution with Lo's scheme

We next simulate the evolution of damage field corresponding to an air-filled surface crevasse in a land-terminating glacier using the Lo's scheme for crack driving force. We define the pre-damaged zone at $x_s^0 = 250$ m with depth $d_s^0 = 0.08H = 10$ m, and then conduct the simulation for 100 pseudo time steps to examine the evolution of the phase field damage variable and predict final depths of surface crevasses.

The damage fields of grounded glaciers predicted by the Lo's scheme is plotted in Fig. 5(a). It shows the localization of damage with a crack-like feature propagating to a final depth $d_s = 0.955H$, which is consistent with the LEFM model result. We also notice that a second crack-like feature nucleates and propagates near the left edge of the domain. The left crack seems to develop as the central crack ceases to propagate, illustrating the ability of the PFM to capture crevasse initiation. Thus, the PFM can be an indispensable approach for understanding the fracture mechanics of closely-spaced glacier crevasses that are widely observed [1]. However, in this study our aim is to verify the PFM with the LEFM model for isolated crevasses by comparing the predicted maximum (or final) depth, and then examine the conditions that enable the full-depth penetration under different meltwater and seawater conditions. Therefore, to promote the localized propagation of an isolated surface crevasse at the pre-damaged zone (i.e. $x_s^0 = 250$ m) and to prevent the initiation of surface crevasses elsewhere, we decreased ℓ_c to 0.1 m. This is equivalent to assuming the cohesive strength σ_c of glacier ice to be 0.2962 MPa, so that damage evolution can only occur at pre-damaged zone due to the local stress concentration. Fig. 5(b) shows the final damage field based on the Lo's scheme with $\ell_c = 0.1$ m at the pseudo time step $n = 100$. The maximum penetration depth of this surface crevasse is predicted to be $d_s = 0.949H$, which shows good agreement with the previous result $d_s = 0.955H$ for $\ell_c = 0.625$ m. This study suggests that the choice of the larger length scale does not affect the predicted maximum crevasse depth, although it alters the width of the damage zone and nucleation of damage elsewhere.

Upon comparing Fig. 5(a) to (b), we find that the final damage field with smaller length scale is more localized and resembles an isolated surface crevasse. Because this corresponds to the assumption of larger cohesive strength of glacier ice, this suppresses the initiation of damage except near the pre-damaged zone. However, a significant drawback of decreasing ℓ_c is the increased computational burden arising from the need to resolve the damage zone with an extremely fine mesh. For the sake of numerical accuracy of the PFM, it is customary that the finite element mesh size be sufficiently smaller than the chosen length scale. Consequently, defining $\ell_c = 0.1$ can be unnecessarily burdensome for evaluating the depth/height of glacier crevasses. In this work, we implement a somewhat *ad hoc* approach to localize the surface crevasse at the pre-damaged zone by assuming a threshold $\mathcal{F}^{\text{th}}$ for the crack driving force. Specifically, at each pseudo time step, we evaluate the crack driving force $\mathcal{H}/\mathcal{G}_c$ at each integration point using the Lo's scheme and set it to zero if $\mathcal{H}/\mathcal{G}_c \leq \mathcal{F}^{\text{th}}$. Our approach is inspired by that of Miehe et al. [62], where an energetic criterion with a threshold was proposed to avoid damage nucleation at lower stress levels.

Here, we define the value of $\mathcal{F}^{\text{th}}$ equal to the maximum crack driving force calculated based on the stress state of the undamaged glacier; therefore, its calibration is valid only for the specific glacier geometry and boundary conditions. The thresholds assumed for grounded glaciers with different seawater levels at terminus in this study are listed in Table 2. Note that for a near-floatation grounded glacier (i.e., $h_w = 0.9H$), $\mathcal{F}^{\text{th}} = 0$ because the compressive seawater pressure at the terminus nullifies the crack driving force in the far-field region of the glacier. With the threshold applied, the final damage field corresponding to an air-filled surface crevasse in a land-terminating glacier looks like an inverted teardrop as shown in Fig. 5(c), which may not be physical; however, the predicted maximum penetration depth $d_s = 0.953H$ is consistent with the LEFM model. The application of threshold $\mathcal{F}^{\text{th}} = 3.271$ successfully localizes the propagation of the crevasse near the assumed pre-damaged region. To test the sensitivity of the predicted maximum depth to the threshold value, we assumed the threshold as $\mathcal{F}^{\text{th}} = 32.71$ (i.e. ten-fold increase). As shown in Fig. 5(d), the width of the damaged zone decreases significantly, but the predicted maximum depth remains at $d_s = 0.953H$, indicating its insensitivity.

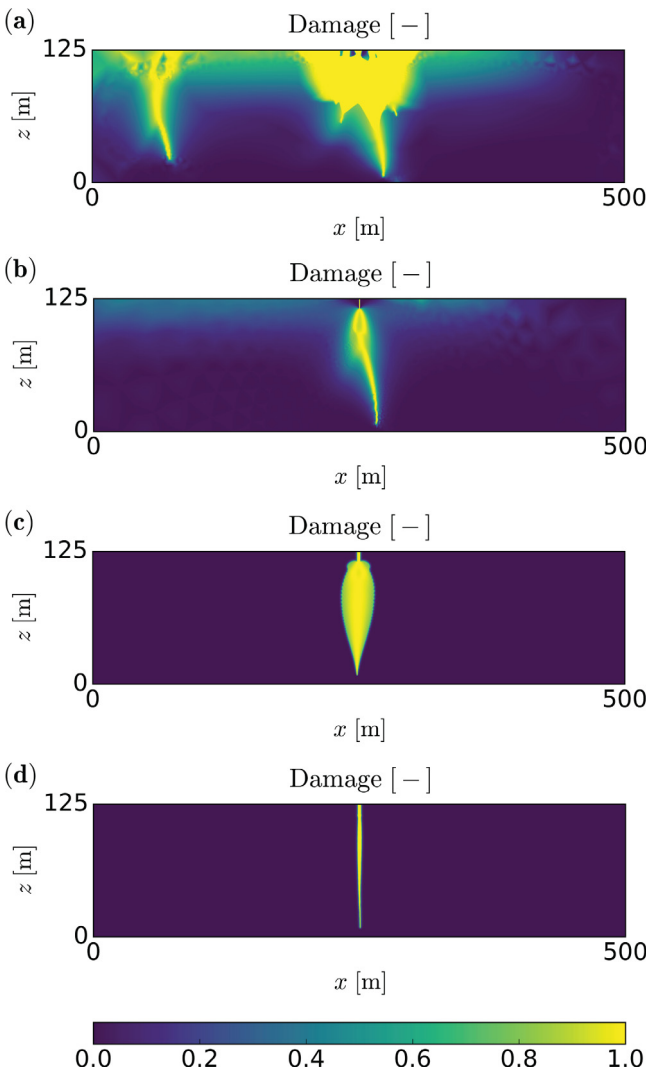

Fig. 5. Final damage fields predicted by PFM using the Lo's scheme for an air-filled surface crevasse (i.e., $h_s = 0$) in a land-terminating glacier with: (a) $\ell_c = 0.625$ m; (b) $\ell_c = 0.1$; (c) $\ell_c = 0.625$ m and $\mathcal{F} = 3.271$; (d) $\ell_c = 0.625$ m and $\mathcal{F} = 32.71$.

3.4. Comparison with the LEFM model

We next assess the accuracy of the proposed poro-damage PFM for estimating the maximum crevasse penetration depth

Table 2
Thresholds of crack driving force for grounded glaciers with different seawater level at terminus.

h_w/H	0%	50%	90%
$\mathcal{F}^{th}$	3.271	0.754	0

relative to that obtained from the LEFM model. Fig. 6 shows the normalized final crevasse depths d_s/H for isolated surface crevasses filled with freshwater to different levels, $h_s/d_s = \{0, 12.5, 25, 37.5, 50, 62.5, 75, 87.5, 100\}$%, within grounded glaciers terminating at the ocean with varying sea levels, $h_w/H = \{0, 50, 90\}$%. As before, surface crevasses are initiated by a pre-damaged zone at $x_s^0 = 250$ m with depth $d_s^0 = 0.08H = 10$ m. Following the studies in the previous section, we use the Lo's scheme with the threshold to calculate crack driving force and take $\ell_c = 0.625$ m to manage the computational cost. The LEFM model results are obtained using the symmetric double edge-cracked plate weight functions as detailed in Appendix C. From Fig. 6, it is evident that the PFM results are in excellent agreement with those from the LEFM model for all cases.

In the case of the land-terminating glaciers (i.e., $h_w = 0$) with free slip at the base, an air-filled surface crevasse can propagate to 95.5% of the thickness of glacier. This is because the lack of compressive seawater pressure acting on the terminus along with the free slip basal condition allows the glacier to flow fast and generate large tensile stress and crack driving force. However, this case is rarely observed in reality owing to a complex interplay between basal friction, basal surface topology, and subglacial water pressure. As the seawater level at terminus is increased, the propagation of surface crevasses requires the presence of meltwater to trigger hydrofracturing. For example, a surface crevasse in a marine-terminating grounded glacier with seawater level $h_w/H = 50$% can propagate to 65% of the glacier thickness if it is partially filled with meltwater ($h_s = 0.375d_s$). The same crevasse if filled with more meltwater ($h_s/d_s \geq 50$%) can penetrate the entire thickness of the marine-terminating glacier, leading to iceberg calving. However, in a grounded marine-terminating glacier that is near-floating (i.e., $h_w/H \approx 90$%), the propagation of surface crevasse is arrested even if there is enough meltwater to fully-fill the crevasse. The above study leads us to the conclusion that a near-floatation glacier is less vulnerable to hydrofracturing and consequent iceberg calving, owing to the compressive seawater pressure at the terminus.

3.5. Cliff failure of near-floatation grounded glaciers

We examine the propagation of an isolated water-filled surface crevasse in the terminus region of a near-floatation grounded glacier (i.e., $h_w/H \approx 90$%). As shown in Fig. 7(a), we define the pre-damaged zone at $x_s^0 = 475$ m with depth $d_s^0 = 0.08H = 10$ m, and assume the meltwater level within the crevasse $h_s/d_s = 100$%. We conduct the simulation for 60 pseudo time steps to demonstrate cliff failure that resembles slumping. As shown in Fig. 7(b), the fully water-filled isolated surface crevasse at the terminus of the near-floatation glacier can propagate and form a curved crack-like feature, which leads to cliff failure and iceberg calving. We find that this failure is driven by both hydrofracturing and considerable in-plane shear stress near the glacier terminus. However, if we assume that crevasse is air-filled (i.e., $h_s/d_s = 0$), we do not see any damage evolution or cliff failure.

We next consider the plausibility of a self-sustaining retreat of the ice terminus, based on the hypothesis of marine ice cliff instability [10,63]. As shown in Fig. 8(a), we define two pre-damaged zones at $x_s^0 = 425$ and 475 m, respectively, with the same depth $d_s^0 = 0.08H = 10$ m. To demonstrate the progressive

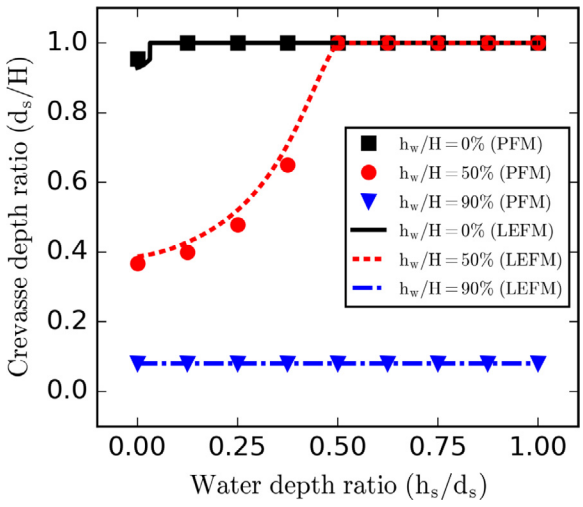

Fig. 6. Surface crevasse depth d_s normalized with the domain height $H = 125$ m for varying freshwater levels h_s filling the surface crevasse within grounded glaciers. The solid and dashed lines depict the 'double edge cracks' LEFM model result for different seawater depths h_w at the terminus. The markers (i.e. black squares, red dots, and blue triangles) represent phase field method (PFM) results based on strain energy decomposition scheme proposed by Lo et al. [38] with threshold $\mathcal{F}^{th}$ applied.

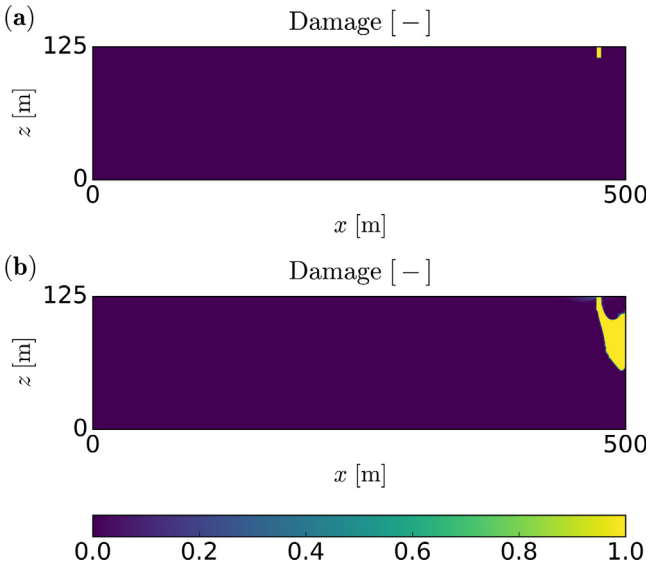

Fig. 7. Damage fields of a near-floatation grounded glacier with an isolated surface crevasse near the right terminus: (a) initial condition; (b) prediction at pseudo time step $n = 100$ using PFM based on the Lo's scheme.

propagation of two fully water-filled crevasses near the terminus, we conduct the simulation for 300 pseudo time steps. We observe three stages of damage evolution: (i) the crevasse closer to the terminus propagates and reaches the right terminus that leads to cliff failure and iceberg calving, as in Fig. 8(b); (ii) As the new calving front is established at $x_s^0 = 475$ m, the surface crevasse at $x_s^0 = 425$ m subsequently begins to propagate, as in Fig. 8(c); (iii) Under the action of hydraulic pressure and in-plane shear the crevasse propagates and reaches the new ice terminus leading to another iceberg calving event, as in Fig. 8(d). The movie showing the evolution of damage through the three stages is provided as supplementary material. While cliff failure is hypothesized for ice termini that are 100 m or more taller over the sea level, our study indicates that hydrofracture can lead to the failure of much shorter cliffs. However, this study does not represent failure

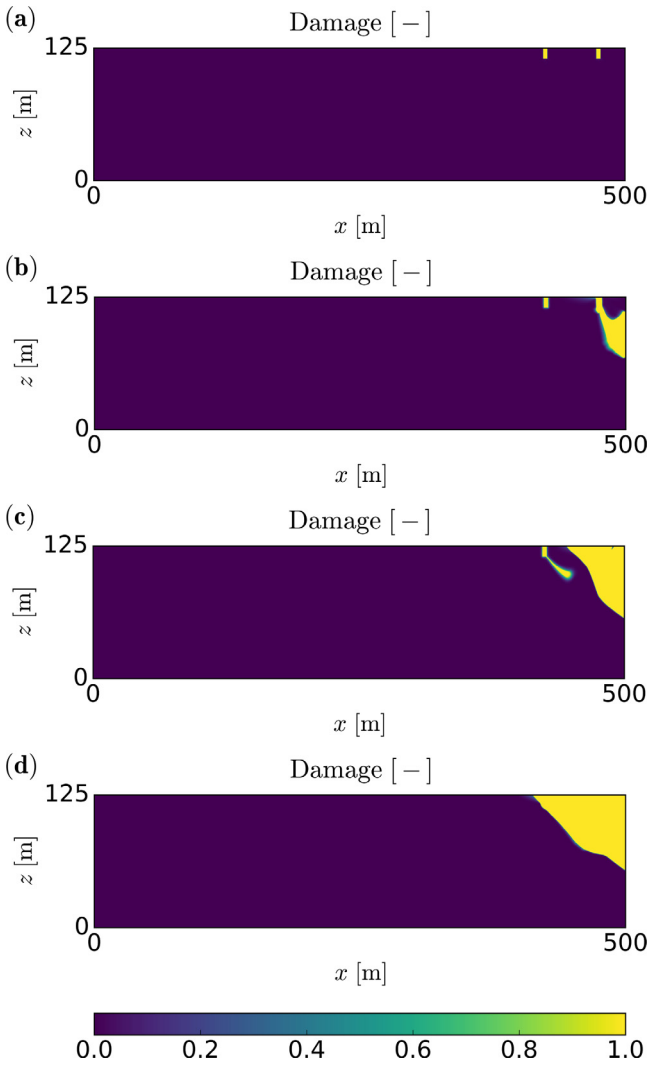

Fig. 8. Damage fields of a near-floatation grounded glacier with two surface crevasses near the right terminus predicted by PFM using the Lo's scheme at different pseudo time steps: (a) $n = 0$; (b) $n = 60$; (c) $n = 220$; (d) $n = 275$.

at the terminus of floating ice shelves and does not consider the effect of buoyancy force that pushes the entire glacier up to floatation. Therefore, further studies are needed that consider realistic glacier geometry and basal boundary condition to better understand the plausibility of marine ice cliff instability.

In Figs. 7 and 8, we see that the damage zone thickness is larger than the length scale parameter. This is because damage evolution is driven by a multi-axial stress state near the terminus of a glacier due to internal body force (self-weight), which causes both normal and shear stresses (see Fig. 3. We acknowledge that our current phase field model with the crack energy density in Eq. (7) may not be appropriate and that modifications are necessary to handle mixed-mode fracture to accurately represent the opening (mode I) and sliding (mode II) mechanisms at the terminus. As evident from the movie provided as supplementary material, at time step 35 the damage zone looks like a crack emanating from the notch closest to the terminus. By time step 50 the damage zone thickness increase and it curves to reach the terminus, thus causing an ice block above the crack to slide off into the ocean and giving birth to a small iceberg. However, we made major simplifications in conducting this preliminary simulation study: (i) we considered the physical status of the fully damage zone to be water, that is, as ice fails we assumed that it gets converted to water in the damage zone; (ii) we ignore mass conservation as the meltwater seeping into the damaged zone alters the amount of mass in the simulation region, and currently we do not track the volume of meltwater; (iii) we do not model the flow of meltwater out of the damage zone in to the seawater, and instead apply the hydrostatic pressure on crack surface. Thus, the weight of the iceberg above the crack is still there, but the density of meltwater in the damage zone applies hydrostatic pressure causing the iceberg to float up. We acknowledge that improvements can be made in representing the mixed-mode nature of fracture and the physical state of ice in the failure zone, but here wish to simply demonstrate the potential of the phase field model to describe progressive crack propagation and the plausibility of marine ice cliff instability.

4. Conclusions

In this paper, we present a poro-damage phase field model (PFM) for hydrofracturing and use it to simulate the propagation of air-filled or water-filled crevasses in grounded glaciers. Assuming glacier ice to be a brittle, compressible, linear elastic solid, the displacement and damage fields are solved in a staggered manner using the standard finite element method in the open-source software FEniCS. Three elastic strain energy decomposition schemes are implemented to calculate the crack driving force (or history field variable) that were proposed by Miehe et al. [33], Zhang et al. [39], and Lo et al. [38], respectively. The maximum penetration depths of crevasses in grounded glaciers evaluated from the poro-damage PFM are compared to the corresponding predictions from the linear elastic fracture mechanics (LEFM) model. The results of our study reveal several important findings relevant to the broader mechanics and earth science community:

1. The crack driving force calculated using the schemes proposed by Miehe et al. and Zhang et al. allow damage accumulation in regions where the longitudinal normal stress is compressive. This contradicts the LEFM result as it violates the tension–compression asymmetry of damage evolution normally assumed for brittle materials;
2. The modified strain energy decomposition scheme proposed by Lo et al. nullifies the crack driving force in regions where the longitudinal stress is compressive, thus leading to an accurate description of brittle fracture, especially in geological media that are subjected to self-gravitational load;
3. For land- and marine-terminating grounded glaciers, applying a sufficiently large threshold on crack driving force calculated using Lo's scheme is an effective (but *ad hoc*) approach to localize the propagation of crevasses at the pre-damaged zone without significantly affecting the prediction of their final depths;
4. The maximum penetration depths of air- and water-filled surface crevasses within grounded glaciers predicted using PFM are in good agreement with those evaluated based on double edge crack LEFM model;
5. In a near-floatation grounded glacier, an isolated surface crevasse in the far-field region may not propagate, despite the level of meltwater filling the crevasse. However, water-filled surface crevasses in the terminus region can propagate progressively and lead to iceberg calving events, owing to hydrofracturing and in-plane shear stress.

In conclusion, the poro-damage PFM based on the strain energy decomposition scheme proposed by Lo et al. [38] can capture the tension–compression asymmetry and simulate glacier crevasses propagation resulting from hydraulic pressure and self-gravitational load in an accurate and efficient manner. However,

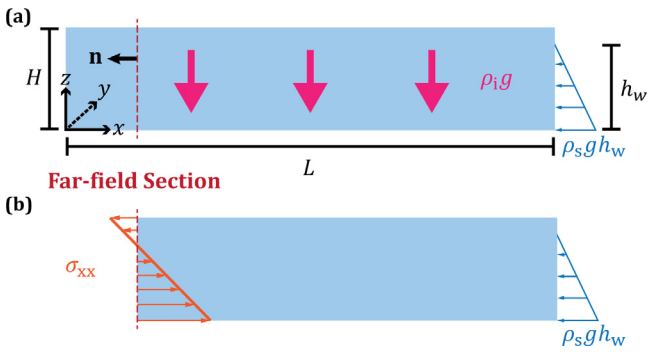

Fig. A.1. (a) Schematic diagram of the floating ice shelf ($L \gg H$) with no tangential traction at the base. A body force with magnitude $-\rho_i g$ in the z-direction is applied as the gravity loading. And a hydrostatic load with hydraulic head h_w is applied to the right terminus of the ice shelf as a depth-varying (triangularly) distributed load. The out-of-plane direction is denoted by y; (b) Free body diagram of forces in x-direction applied on the far-field section of the ice shelf cut at the red dashed line with the surface normal vector denoted by $\boldsymbol{n}$.

the current PFM model is based on the assumption of compressible linear elastic behavior of glacier ice, which does not represent the deformational flow over long timescales as observed from field studies and satellite imaging [64]. In fact, glacier ice is generally considered as visco-elastic/plastic material, so further developments of the poro-damage PFM are necessary to account for rate-dependent mechanical and fracture responses [65]. Our future work will focus on both extending the current poro-damage PFM for viscoelastic ice, and applying it to real glaciers to better understand the fracture behavior of glaciers in response to atmospheric warming and surface meltwater production.

Declaration of competing interest

The authors declare that they have no known competing financial interests or personal relationships that could have appeared to influence the work reported in this paper.

Acknowledgment

We gratefully acknowledge the funding support provided by the National Science Foundation's Office of Polar Programs, USA via grants #PLR-1341428 and #PLR-1847173.

Appendix A. Derivation of the far-field longitudinal (horizontal) normal stress σ_{xx}

We consider a freely floating ice shelf (i.e., no tangential traction at the base) under plane strain assumptions, as depicted in Fig. A.1(a). A body force with magnitude of $-\rho_i g$ in the z-direction is applied as the gravity loading. And a hydrostatic load with hydraulic head h_w is applied to the right terminus of the ice shelf as a depth-varying (triangularly) distributed load. Under such circumstance, we have the far-field equilibrium equations in three dimensions as given by

$$\begin{cases} \frac{\partial \sigma_{xx}}{\partial x} + \frac{\partial \sigma_{xy}}{\partial y} + \frac{\partial \sigma_{xz}}{\partial z} = 0, \\ \frac{\partial \sigma_{xy}}{\partial x} + \frac{\partial \sigma_{yy}}{\partial y} + \frac{\partial \sigma_{yz}}{\partial z} = 0, \\ \frac{\partial \sigma_{zx}}{\partial x} + \frac{\partial \sigma_{zy}}{\partial y} + \frac{\partial \sigma_{zz}}{\partial z} + \rho_i g = 0. \end{cases} \tag{A.1}$$

We assume that far-field stresses are invariant with x-coordinate and out-of-plane stresses are zero. We can now simplify Eq. (A.1) as

$$\begin{cases} \frac{\partial \sigma_{xy}}{\partial y} = 0, \\ \frac{\partial \sigma_{yy}}{\partial y} = 0, \\ \frac{\partial \sigma_{zz}}{\partial z} + \rho_i g = 0. \end{cases} \tag{A.2}$$

At z-direction, we can solve the stress component σ_{zz} based on the feature of gravitational loading. The corresponding boundary conditions for Eq. (A.2c) can be expressed as

$$\begin{cases} \sigma_{zz} = -\rho_i g H & \text{at } z = 0, \\ \sigma_{zz} = 0 & \text{at } z = H. \end{cases} \tag{A.3}$$

Therefore, the vertical normal stress σ_{zz} can be expressed as

$$\sigma_{zz}(z) = -\rho_i g\,(H - z)\,. \tag{A.4}$$

Based on the theory of compressible linear elasticity, we have the constitutive relations as given by

$$\begin{cases} \varepsilon_{xx} = \frac{1}{E}\left[\sigma_{xx} - \nu\left(\sigma_{yy} + \sigma_{zz}\right)\right], \\ \varepsilon_{yy} = \frac{1}{E}\left[\sigma_{yy} - \nu\left(\sigma_{xx} + \sigma_{zz}\right)\right], \\ \varepsilon_{zz} = \frac{1}{E}\left[\sigma_{zz} - \nu\left(\sigma_{xx} + \sigma_{yy}\right)\right]. \end{cases} \tag{A.5}$$

Based on the plane strain assumption (i.e., $\varepsilon_{yy} = 0$), we can further simplify Eq. (A.5b) as

$$\sigma_{yy} = \nu\left(\sigma_{xx} + \sigma_{zz}\right). \tag{A.6}$$

Upon substituting Eq. (A.6) into Eq. (A.5a), we have

$$\varepsilon_{xx} = \frac{1}{E}\left[\left(1 - \nu^2\right)\sigma_{xx} - \nu\left(1 + \nu\right)\sigma_{zz}\right]. \tag{A.7}$$

Furthermore, the length of typical ice shelves is at the level of kilometers, whereas its thickness is at the level of hundred meters. Therefore, we here adopt the membrance stress assumption based on the geometric feature of glaciers. The horizontal displacement is then assumed to be vertically invariant, which can be expressed as

$$\frac{\partial u}{\partial z} = \frac{\partial v}{\partial z} = 0 \implies \frac{\partial}{\partial x}\left(\frac{\partial u}{\partial z}\right) = 0. \tag{A.8}$$

The above partial derivative is interchangeable, we thus have

$$\frac{\partial}{\partial z}\left(\frac{\partial u}{\partial x}\right) = 0 \implies \frac{\partial \varepsilon_{xx}}{\partial z} = 0, \tag{A.9}$$

which means the horizontal strain component is depth invariant. Upon taking derivative on both sides of Eq. (A.7) with z and simplifying it based on Eq. (A.9), we have

$$\frac{\partial \sigma_{xx}}{\partial z} = \frac{\nu}{1 - \nu}\frac{\partial \sigma_{zz}}{\partial z}. \tag{A.10}$$

Combining Eqs. (A.10) and (A.2c), we have

$$\frac{\partial \sigma_{xx}}{\partial z} = -\frac{\nu}{1 - \nu}\rho_i g. \tag{A.11}$$

We know that far-field stresses are invariant with x-coordinate and for the plane strain problem

$$\frac{\partial \sigma_{xx}}{\partial y} = 0. \tag{A.12}$$

Therefore, the stress component σ_{xx} is only dependent on z-coordinate. Eq. (A.11) can be integrated with respect to z as

$$\sigma_{xx} = -\frac{\nu}{1 - \nu}\rho_i g z + C, \tag{A.13}$$

where C is an unknown constant. We next consider the force balance in x-direction based on the free body diagram of a far-field section of the floating ice shelf cut at the red dashed line, as

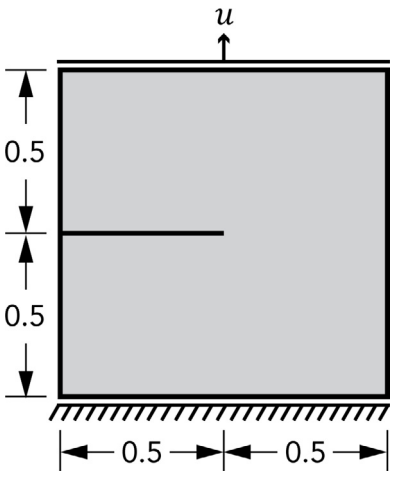

Fig. B.1. Geometry and boundary conditions of a square single edge notched specimen subjected to tensile loading.

shown in Fig. A.1(b). The equilibrium equation in x-direction can be written as

$$\sum F_x = \int_0^H \sigma_{xx} dz + F_w = 0, \tag{A.14}$$

where $F_w = \frac{1}{2}\rho_s g h_w^2$ is the resultant force caused by the hydrostatic load. Substituting Eq. (A.13) into Eq. (A.14), we have

$$C = \frac{\nu}{2(1-\nu)}\rho_i g H - \frac{1}{2}\rho_s g \frac{h_w^2}{H}. \tag{A.15}$$

Combining Eqs. (A.13) and (A.15), we have the expression of far-field longitudinal normal stress through ice thickness as

$$\sigma_{xx} = \frac{\nu}{1-\nu}\left[\frac{1}{2}\rho_i g H - \rho_i g\,(H-z)\right] - \frac{1}{2}\rho_s g \frac{h_w^2}{H}. \tag{A.16}$$

Appendix B. Numerical verification study: Single edge notched tension test

To verify our staggered implementation of the hybrid phase field model introduced in Section 2.1, we conduct a standard benchmark study of the single edge notched specimen subjected to tensile loading. As shown in Fig. B.1, we consider a square plate containing a horizontal notch with a length of 0.5 mm located at mid-height of the left boundary. The specimen is pinned at the bottom and tensile loading is realized by a monotonic displacement u applied on the top boundary.

The parameters of material properties and phase field model are chosen to be the same as those used in [33], as listed in Table B.1. We consider three different strain energy decomposition schemes proposed by Miehe et al. [33], Zhang et al. [39], and Lo et al. [38], respectively. Note that for Zhang's scheme, the critical strain energy release rate for mode I fracture $\mathcal{G}_{Ic}$ is taken as the same value of $\mathcal{G}_c$ listed in Table B.1. The displacement control is applied with a constant increment $\Delta u = 10^{-5}$ mm in the first 500 time steps. After that, the displacement increment is adjusted to 10^{-6} mm owing to the rapid propagation of the crack.

Fig. B.2 shows three load–displacement curves obtained from phase field modeling based on corresponding strain energy decomposition schemes. The benchmark solution is plotted as black circular markers, which is digitized from Figure 9 of [34]. The results computed from our models using Miehe's and Lo's schemes are in good agreement with the benchmark solution; whereas, the discrepancy between the benchmark solution and the result obtained using Zhang's scheme is caused by the choice of critical strain energy release rate for mode II fracture $\mathcal{G}_{IIc} = 10\mathcal{G}_{Ic}$.

Table B.1
Parameters of material properties and phase field modeling of single edged notch tension test.

Parameter	Value	Unit
λ	121.5	kN/mm^2
μ	80.7	kN/mm^2
$\mathcal{G}_c$	2.7×10^{-3}	kN/mm
ℓ_c	0.015	mm
η	10^{-6}	kN s/m^2

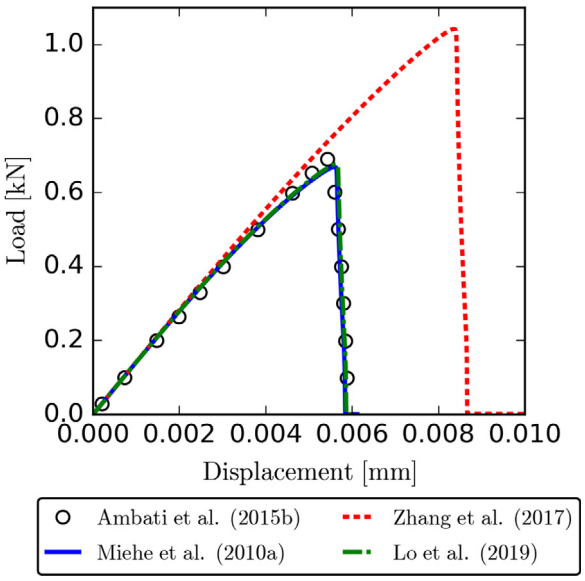

Fig. B.2. Load–displacement curves for single edge notched tension test. The solid and dashed lines depict the numerical results obtained from phase field model based on the corresponding strain energy decomposition schemes. The black circular maker represents the benchmark solution digitized from Figure 9 of [34].

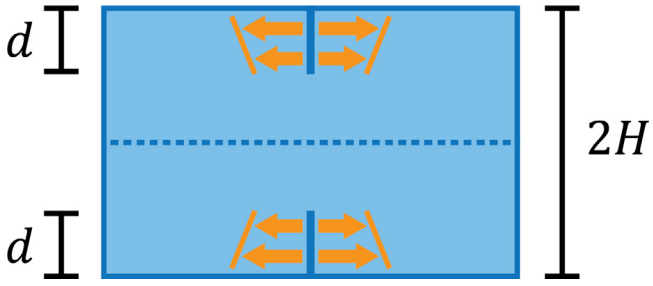

Fig. C.1. Double edge cracks through finite slabs with H in width and d in crack length. The yellow arrows indicate applied loading on the crack surface that leads to crack opening. The dashed line of symmetry represents the free slip surface at the base of the glacier.

Appendix C. LEFM model applied to predict the maximum penetration depths of crevasses

The LEFM models proposed in previous studies [4,15–17] are ideally suited for a rectangular plate-like glacier made of linear elastic ice with a single edge crack subjected to the far-field longitudinal normal stress given by Eq. (A.16). In this paper, we consider the scenario of surface crevasse propagation in grounded glaciers. The double edge cracks can approximate a surface crevasse in a grounded glacier with free tangential slip, as shown in Fig. C.1(a).

In LEFM models, the crack propagation is governed by the stress intensity factor (SIF) at the crack tip, which depends on the

applied far-field stress and the initial crack length. The maximum penetration depth of crevasses can be determined by equating the mode I net SIF $K_{\mathrm{I}}^{\mathrm{net}}$ at the crevasse tip to the experimentally measured critical SIF of ice $K_{\mathrm{Ic}} = 0.1$ MPa $\mathrm{m}^{\frac{1}{2}}$. The mode I net SIF can be evaluated as

$$K_{\mathrm{I}}^{\mathrm{net}} = \int_0^d M(\zeta, H, d)\sigma_{\mathrm{net}}(\zeta)\mathrm{d}\zeta, \tag{C.1}$$

where $M(\zeta, H, d)$ is an appropriate weight function for specific geometry and boundary conditions, and σ_{net} is the net longitudinal stress that leads to crevasse opening, which can be expressed as [66–68]

$$\sigma_{\mathrm{net}}(z) = \sigma_{\mathrm{xx}}(z) + p_{\mathrm{w}}(z), \tag{C.2}$$

where the hydraulic pressure p_{w} is given by Eq. (16). The weight function for the double edge cracks LEFM model has been given in [69] as

$$M_{\mathrm{D}}(\zeta, H, d) = \frac{2}{\sqrt{2H}}\left[1 + f_1\left(\frac{\zeta}{d}\right) f_2\left(\frac{d}{H}\right)\right]\phi\left(\frac{d}{H}, \frac{\zeta}{H}\right), \tag{C.3}$$

where $d = d_{\mathrm{s}}$ and $\zeta = H - z$ for surface crevasses, and the function f_1 is given as

$$f_1\left(\frac{\zeta}{d}\right) = 0.3\left[1 - \left(\frac{\zeta}{d}\right)^{5/4}\right], \tag{C.4}$$

and the function f_2 is given as

$$f_2\left(\frac{d}{H}\right) = \frac{1}{2}\left[1 - \sin\left(\frac{\pi d}{2H}\right)\right]\left[2 + \sin\left(\frac{\pi d}{2H}\right)\right], \tag{C.5}$$

and the function ϕ is given as

$$\phi\left(\frac{d}{H}, \frac{\zeta}{H}\right) = \frac{\sqrt{\tan\left(\frac{\pi d}{2H}\right)}}{\sqrt{1 - \left[\cos\left(\frac{\pi d}{2H}\right)/\cos\left(\frac{\pi \zeta}{2H}\right)\right]^2}}. \tag{C.6}$$

To obtain the LEFM predicted final depths of crevasses as plotted in Fig. 6, we next equate the mode I net SIF evaluated using Eq. (C.1) to the experimentally determined critical SIF. These nonlinear equations with the unknowns of maximum penetration depths are solved using an iterative algorithm based on the bisection method.

Appendix D. Supplementary data

Supplementary material related to this article can be found online at https://doi.org/10.1016/j.eml.2021.101277.

References

[1] W. Colgan, H. Rajaram, W. Abdalati, C. McCutchan, R. Mottram, M.S. Moussavi, S. Grigsby, Glacier crevasses: Observations, models, and mass balance implications, Rev. Geophys. 54 (1) (2016) 119–161.

[2] E.M. Enderlin, T.C. Bartholomaus, Sharp contrasts in observed and modeled crevasse patterns at greenland's marine terminating glaciers, Cryosphere 14 (11) (2020) 4121–4133.

[3] J. Weertman, Can a water-filled crevasse reach the bottom surface of a glacier, IASH Publ. 95 (1973) 139–145.

[4] C. Van der Veen, Fracture mechanics approach to penetration of surface crevasses on glaciers, Cold Reg. Sci. Technol. 27 (1) (1998) 31–47.

[5] D.I. Benn, C.R. Warren, R.H. Mottram, Calving processes and the dynamics of calving glaciers, Earth Sci. Rev. 82 (3–4) (2007) 143–179.

[6] R.B. Alley, T.K. Dupont, B.R. Parizek, S. Anandakrishnan, Access of surface meltwater to beds of sub-freezing glaciers: preliminary insights, Ann. Glaciol. 40 (2005) 8–14.

[7] D. Lampkin, N. Amador, B. Parizek, K. Farness, K. Jezek, Drainage from water-filled crevasses along the margins of Jakobshavn Isbræ: A potential catalyst for catchment expansion, J. Geophys. Res. Solid Earth 118 (2) (2013) 795–813.

[8] P.A. Tuckett, J.C. Ely, A.J. Sole, S.J. Livingstone, B.J. Davison, J.M. van Wessem, J. Howard, Rapid accelerations of antarctic peninsula outlet glaciers driven by surface melt, Nature Commun. 10 (1) (2019) 1–8.

[9] K. Poinar, I. Joughin, S.B. Das, M.D. Behn, J.T. Lenaerts, M.R. Van Den Broeke, Limits to future expansion of surface-melt-enhanced ice flow into the interior of western greenland, Geophys. Res. Lett. 42 (6) (2015) 1800–1807.

[10] R.M. DeConto, D. Pollard, Contribution of antarctica to past and future sea-level rise, Nature 531 (7596) (2016) 591–597.

[11] H.-O. Pörtner, D.C. Roberts, V. Masson-Delmotte, P. Zhai, M. Tignor, E. Poloczanska, K. Mintenbeck, M. Nicolai, A. Okem, J. Petzold, et al., Ipcc special report on the ocean and cryosphere in a changing climate, in: IPCC Intergovernmental Panel on Climate Change (IPCC), 2019.

[12] M.E. Mobasher, R. Duddu, J.N. Bassis, H. Waisman, Modeling hydraulic fracture of glaciers using continuum damage mechanics, J. Glaciol. 62 (234) (2016) 794–804.

[13] D. Santillán, R. Juanes, L. Cueto-Felgueroso, Phase field model of hydraulic fracturing in poroelastic media: Fracture propagation, arrest, and branching under fluid injection and extraction, J. Geophys. Res. Solid Earth 123 (3) (2018) 2127–2155.

[14] L. Ultee, C. Meyer, B. Minchew, Tensile strength of glacial ice deduced from observations of the 2015 eastern Skaftá cauldron collapse, Vatnajökull ice cap, Iceland, J. Glaciol. (2020) 1–10.

[15] R. Smith, The application of fracture mechanics to the problem of crevasse penetration, J. Glaciol. 17 (76) (1976) 223–228.

[16] C. Van der Veen, Fracture mechanics approach to penetration of bottom crevasses on glaciers, Cold Reg. Sci. Technol. 27 (3) (1998) 213–223.

[17] J. Krug, J. Weiss, O. Gagliardini, G. Durand, Combining damage and fracture mechanics to model calving, Cryosphere 8 (6) (2014) 2101–2117.

[18] H. Yu, E. Rignot, M. Morlighem, H. Seroussi, Iceberg calving of thwaites glacier, west antarctica: full-Stokes modeling combined with linear elastic fracture mechanics, Cryosphere 11 (3) (2017) 1283.

[19] C.-Y. Lai, J. Kingslake, M.G. Wearing, P.-H.C. Chen, P. Gentine, H. Li, J.J. Spergel, J.M. van Wessem, Vulnerability of antarctica's ice shelves to meltwater-driven fracture, Nature 584 (7822) (2020) 574–578.

[20] S. Jiménez, R. Duddu, On the evaluation of the stress intensity factor in calving models using linear elastic fracture mechanics, J. Glaciol. 64 (247) (2018) 759–770.

[21] G.A. Francfort, J.-J. Marigo, Revisiting brittle fracture as an energy minimization problem, J. Mech. Phys. Solids 46 (8) (1998) 1319–1342.

[22] P.-O. Bouchard, F. Bay, Y. Chastel, Numerical modelling of crack propagation: automatic remeshing and comparison of different criteria, Comput. Methods Appl. Mech. Eng. 192 (35–36) (2003) 3887–3908.

[23] P. Dumstorff, G. Meschke, Crack propagation criteria in the framework of X-FEM-based structural analyses, Int. J. Numer. Anal. Methods Geomech. 31 (2) (2007) 239–259.

[24] S. Bordas, T. Rabczuk, G. Zi, Three-dimensional crack initiation, propagation, branching and junction in non-linear materials by an extended meshfree method without asymptotic enrichment, Eng. Fract. Mech. 75 (5) (2008) 943–960.

[25] N. Sukumar, D.L. Chopp, E. Béchet, N. Moës, Three-dimensional non-planar crack growth by a coupled extended finite element and fast marching method, Internat. J. Numer. Methods Engrg. 76 (5) (2008) 727–748.

[26] P. Gupta, C.A. Duarte, A. Dhankhar, Accuracy and robustness of stress intensity factor extraction methods for the generalized/extended finite element method, Eng. Fract. Mech. 179 (2017) 120–153.

[27] C. Song, E.T. Ooi, S. Natarajan, A review of the scaled boundary finite element method for two-dimensional linear elastic fracture mechanics, Eng. Fract. Mech. 187 (2018) 45–73.

[28] B. Mazurowski, A. Sanchez-Rivadeneira, N. Shauer, C. Duarte, High-order stable generalized/extended finite element approximations for accurate stress intensity factors, Eng. Fract. Mech. (2020) 107308.

[29] B. Bourdin, G.A. Francfort, J.-J. Marigo, Numerical experiments in revisited brittle fracture, J. Mech. Phys. Solids 48 (4) (2000) 797–826.

[30] A. Griffith, The phenomena of rupture and flow in solids, Phil. Trans. R. Soc. Lond. 221 (1921) 163–198.

[31] C. Miehe, F. Welschinger, M. Hofacker, Thermodynamically consistent phase-field models of fracture: Variational principles and multi-field FE implementations, Int. J. Numer. Methods Eng. 83 (10) (2010) 1273–1311.

[32] H. Amor, J.-J. Marigo, C. Maurini, Regularized formulation of the variational brittle fracture with unilateral contact: Numerical experiments, J. Mech. Phys. Solids 57 (8) (2009) 1209–1229.

[33] C. Miehe, M. Hofacker, F. Welschinger, A phase field model for rate-independent crack propagation: Robust algorithmic implementation based on operator splits, Comput. Methods Appl. Mech. Eng. 199 (45–48) (2010) 2765–2778.

[34] M. Ambati, T. Gerasimov, L. De Lorenzis, A review on phase-field models of brittle fracture and a new fast hybrid formulation, Comput. Mech. 55 (2) (2015) 383–405.

[35] C.V. Verhoosel, R. de Borst, A phase-field model for cohesive fracture, Int. J. Numer. Methods Eng. 96 (1) (2013) 43–62.

[36] A. Schlüter, A. Willenbücher, C. Kuhn, R. Müller, Phase field approximation of dynamic brittle fracture, Comput. Mech. 54 (5) (2014) 1141–1161.
[37] H. Ren, X. Zhuang, C. Anitescu, T. Rabczuk, An explicit phase field method for brittle dynamic fracture, Comput. Struct. 217 (2019) 45–56.
[38] Y.-S. Lo, M.J. Borden, K. Ravi-Chandar, C.M. Landis, A phase-field model for fatigue crack growth, J. Mech. Phys. Solids 132 (2019) 103684.
[39] X. Zhang, S.W. Sloan, C. Vignes, D. Sheng, A modification of the phase-field model for mixed mode crack propagation in rock-like materials, Comput. Methods Appl. Mech. Eng. 322 (2017) 123–136.
[40] E.C. Bryant, W. Sun, A mixed-mode phase field fracture model in anisotropic rocks with consistent kinematics, Comput. Methods Appl. Mech. Eng. 342 (2018) 561–584.
[41] J.-Y. Wu, V.P. Nguyen, H. Zhou, Y. Huang, A variationally consistent phase-field anisotropic damage model for fracture, Comput. Methods Appl. Mech. Eng. 358 (2020) 112629.
[42] C. Steinke, M. Kaliske, A phase-field crack model based on directional stress decomposition, Comput. Mech. 63 (5) (2019) 1019–1046.
[43] Q. Wang, Y. Feng, W. Zhou, Y. Cheng, G. Ma, A phase-field model for mixed-mode fracture based on a unified tensile fracture criterion, Comput. Methods Appl. Mech. Eng. 370 (2020) 113270.
[44] S. Zhou, X. Zhuang, T. Rabczuk, Phase field modeling of brittle compressive-shear fractures in rock-like materials: A new driving force and a hybrid formulation, Comput. Methods Appl. Mech. Eng. 355 (2019) 729–752.
[45] B. Bourdin, C.P. Chukwudozie, K. Yoshioka, et al., A variational approach to the numerical simulation of hydraulic fracturing, in: SPE Annual Technical Conference and Exhibition, Society of Petroleum Engineers, 2012.
[46] A. Mikelić, M.F. Wheeler, T. Wick, Phase-field modeling of a fluid-driven fracture in a poroelastic medium, Comput. Geosci. 19 (6) (2015) 1171–1195.
[47] C. Miehe, S. Mauthe, Phase field modeling of fracture in multi-physics problems. Part III. crack driving forces in hydro-poro-elasticity and hydraulic fracturing of fluid-saturated porous media, Comput. Methods Appl. Mech. Eng. 304 (2016) 619–655.
[48] S. Lee, M.F. Wheeler, T. Wick, Pressure and fluid-driven fracture propagation in porous media using an adaptive finite element phase field model, Comput. Methods Appl. Mech. Eng. 305 (2016) 111–132.
[49] Z.A. Wilson, C.M. Landis, Phase-field modeling of hydraulic fracture, J. Mech. Phys. Solids 96 (2016) 264–290.
[50] D. Santillán, R. Juanes, L. Cueto-Felgueroso, Phase field model of fluid-driven fracture in elastic media: Immersed-fracture formulation and validation with analytical solutions, J. Geophys. Res. Solid Earth 122 (4) (2017) 2565–2589.
[51] C. Chukwudozie, B. Bourdin, K. Yoshioka, A variational phase-field model for hydraulic fracturing in porous media, Comput. Methods Appl. Mech. Eng. 347 (2019) 957–982.
[52] S. Zhou, X. Zhuang, T. Rabczuk, Phase field method for quasi-static hydro-fracture in porous media under stress boundary condition considering the effect of initial stress field, Theor. Appl. Fract. Mech. 107 (2020) 102523.
[53] L.-P. Yi, H. Waisman, Z.-Z. Yang, X.-G. Li, A consistent phase field model for hydraulic fracture propagation in poroelastic media, Comput. Methods Appl. Mech. Eng. 372 (2020) 113396.
[54] R. Duddu, S. Jiménez, J. Bassis, A non-local continuum poro-damage mechanics model for hydrofracturing of surface crevasses in grounded glaciers, J. Glaciol. 66 (257) (2020) 415–429.
[55] K. Pham, K. Ravi-Chandar, C. Landis, Experimental validation of a phase-field model for fracture, Int. J. Fract. 205 (1) (2017) 83–101.
[56] M.S. Alnæs, J. Blechta, J. Hake, A. Johansson, B. Kehlet, A. Logg, C. Richardson, J. Ring, M.E. Rognes, G.N. Wells, The FEniCS project version 1.5, Arch. Numer. Softw. 3 (100) (2015) 9–23.
[57] R. Duddu, H. Waisman, A temperature dependent creep damage model for polycrystalline ice, Mech. Mater. 46 (2012) 23–41.
[58] M. Rist, P. Sammonds, S. Murrell, P. Meredith, C. Doake, H. Oerter, K. Matsuki, Experimental and theoretical fracture mechanics applied to Antarctic ice fracture and surface crevassing, J. Geophys. Res. Solid Earth 104 (B2) (1999) 2973–2987.
[59] J. Christmann, R. Müller, K. Webber, D. Isaia, F. Schader, S. Kipfstuhl, J. Freitag, A. Humbert, Measurement of fracture toughness of polycrystalline bubbly ice from an antarctic ice core, Earth Syst. Sci. Data 7 (2015) 87–92.
[60] A. Hillerborg, M. Modéer, P.-E. Petersson, Analysis of crack formation and crack growth in concrete by means of fracture mechanics and finite elements, Cem. Concr. Res. 6 (6) (1976) 773–781.
[61] M.A. Rist, P.R. Sammonds, H. Oerter, C.S.M. Doake, Fracture of antarctic shelf ice, J. Geophys. Res. Solid Earth 107 (B1) (2002) ECV 2–1–ECV 2–13.
[62] C. Miehe, L.-M. Schänzel, H. Ulmer, Phase field modeling of fracture in multi-physics problems. Part i. balance of crack surface and failure criteria for brittle crack propagation in thermo-elastic solids, Comput. Methods Appl. Mech. Eng. 294 (2015) 449–485.
[63] D. Pollard, R.M. DeConto, R.B. Alley, Potential antarctic ice sheet retreat driven by hydrofracturing and ice cliff failure, Earth Planet. Sci. Lett. 412 (2015) 112–121.
[64] K.M. Cuffey, W.S.B. Paterson, The Physics of Glaciers, Academic Press, 2010.
[65] B. Yin, M. Kaliske, Fracture simulation of viscoelastic polymers by the phase-field method, Comput. Mech. 65 (2020) 293–309.
[66] K.C. Jezek, A modified theory of bottom crevasses used as a means for measuring the buttressing effect of ice shelves on inland ice sheets, J. Geophys. Res. Solid Earth 89 (B3) (1984) 1925–1931.
[67] F.M. Nick, C.J. Van der Veen, A. Vieli, D.I. Benn, A physically based calving model applied to marine outlet glaciers and implications for the glacier dynamics, J. Glaciol. 56 (199) (2010) 781–794.
[68] J.N. Bassis, The statistical physics of iceberg calving and the emergence of universal calving laws, J. Glaciol. 57 (201) (2011) 3–16.
[69] H. Tada, P.C. Paris, G.R. Irwin, The Stress Analysis of Cracks Handbook, third ed., ASME Press, 2000.